AIAA JOURNAL
Vol. 40, No. 1, January 2002

Three-Dimensional Numerical Simulation of the Jet Screech Phenomenon

Hao Shen* and Christopher K. W. Tam†
Florida State University, Tallahassee, Florida 32306-4510

Three-dimensional numerical simulations of the jet screech phenomenon are carried out using the multiple-size-mesh, multiple-time-step, dispersion-relation-preserving scheme. The simulations reproduce all of the experimentally observed characteristic features of the screech tones, including the axisymmetric A_1 and A_2 modes, the flapping/helical *B* and *C* modes, and the staging phenomenon. Screech tone frequencies as well as intensities calculated by the numerical simulations are in excellent agreement with experimental measurements. Power spectral analysis of the numerical simulation data provides irrefutable evidence that, whenever two tones are measured in the noise spectrum, it is not because there is a continuous switching from one tone to another, but because the two tones actually coexist simultaneously. A first explanation of why there are two axisymmetric and two flapping/helical screech modes based on two feedback mechanisms is offered. Strong evidence is provided to support the proposed mechanisms.

I. Introduction

NUMERICAL simulations of the jet screech phenomenon are carried out using computational aeroacoustics (CAA) methods. This is an extension of the authors' earlier works on numerical simulation of axisymmetric jet screech tones.[1,2] The present study includes the fully three-dimensional jet screech modes.

Experimental observations[3–7] indicate that jet screech is a fairly complex phenomenon. When a convergent nozzle is used, the screech modes are axisymmetric at low supersonic Mach number. There are two axisymmetric modes. They are usually designated as the A_1 and A_2 modes. At Mach number 1.3 or higher, the jet screech switches to flapping or helical modes. They are referred to as the *B* and *C* modes. Mode switching or staging is quite abrupt. The staging Mach number is found to be very sensitive to ambient conditions of the experiment and probably also very sensitive to the upstream conditions of the jet flow. Largely because of this sensitivity, it is known that the staging Mach numbers differ slightly from experiment to experiment. Even in the same facility, they tend to differ somewhat when the experiment is repeated at a later time.

Jet screech is known to be driven by a feedback loop.[3] The energy is supplied by the instability waves of the jet flow.[8] The phenomenon is highly nonlinear. As a result, even after 40 years of investigation, only approximate screech tone frequency prediction formulas are available.[9–11] The screech tone frequencies of the A_1 and A_2 modes differ only slightly. The same is true with the *B* and *C* modes. The available prediction formulas, unfortunately, are incapable of distinguishing the two modes. For a given Mach number, these formulas predict only a single screech frequency, not two as observed experimentally. Because of the strong nonlinearity of the feedback loop, no one has been able to derive a tone intensity prediction formula. Even a totally empirical formula is not available. Thus, in essence, very little can be done in terms of predicting the screech phenomenon at this time, despite years of research.

The first objective of this investigation is to demonstrate that accurate prediction of the jet screech phenomenon in three dimensions over an extended Mach number range can be done computationally using CAA methods. Here, the entire phenomenon is simulated numerically. One advantage of numerical simulation is that it can readily handle any nonlinearities of the problem. It will be shown that, if a properly designed CAA computational algorithm is used, numerical simulation can provide accurate prediction of the individual frequency of the A_1 and A_2 modes at low supersonic Mach numbers and those of the *B* and *C* modes at higher Mach numbers.

In many ways, numerical simulations may be regarded as numerical experiments. A significant advantage of numerical simulations over physical experiments is that all of the flow and acoustic variables are readily available over the entire computational domain at any instant of time. This allows one to process and examine the physical variables over a reasonably long period of time to better understand the important physics of the phenomenon.

Results of the numerical simulations will be provided in this paper. Below Mach number 1.3, the simulated jet undergoes axisymmetric screech. Depending on the jet Mach number, the feedback loop locks on either the A_1 or A_2 screech mode or both. At Mach 1.3 and higher the screech is associated with a flapping/helical mode. Both the *B* and the *C* modes are observed in the numerical simulations. These behaviors of the simulated jets are consistent with those observed in physical experiments. The simulated jet, just as in the case of a real jet, sometimes locks on two screech modes at the same time. Whenever two screech tones are present simultaneously, one tone is invariably dominant. The measured screech frequencies are found to compare well with the NASA Langley Research Center screech tone data.[6] The intensities of the screech tones are also in good agreement with experimental measurements.

As far as is known, there has never been an explanation as to why there are two axisymmetric jet screech modes, the A_1 and the A_2 modes, or why there are two flapping/helical modes, the *B* and the *C* modes. Here an explanation is given for the first time. It is proposed that the feedback loop, which is responsible for the generation of the screech tones, may be closed in two ways. This results in two slightly different feedback loops and, hence, two slightly different tones. Computed data from the numerical simulations are used to provide crucial evidence to support the proposal.

II. Mathematical Model and Computation Algorithm

The mathematical model and computation algorithm used in this study are quite similar to those used in Refs. 1 and 2. However, because three-dimensional modes are to be simulated, significant extensions of the previous method become necessary. Here, only the important extensions are reported.

A. Mathematical Model

The Reynolds-averaged Navier–Stokes equations (RANS) with the k–ε turbulence model are used for calculating the jet flow and

---

Received 12 October 2000; presented as Paper 2001-0820 at the AIAA 39th Aerospace Sciences Meeting, Reno, NV, 8–11 January 2001; revision received 25 July 2001; accepted for publication 30 July 2001. Copyright © 2001 by Hao Shen and Christopher K. W. Tam. Published by the American Institute of Aeronautics and Astronautics, Inc., with permission. Copies of this paper may be made for personal or internal use, on condition that the copier pay the $10.00 per-copy fee to the Copyright Clearance Center, Inc., 222 Rosewood Drive, Danvers, MA 01923; include the code 0001-1452/02 $10.00 in correspondence with the CCC.

*Postdoctoral Research Associate, Department of Mathematics. Member AIAA.

†Robert O. Lawton Distinguished Professor, Department of Mathematics; tam@math.fsu.edu. Fellow AIAA.

acoustics. The purpose of incorporating the k–ε model in the computation is to simulate the effect of the fine-scale turbulence on the jet flow. The instability wave that drives the feedback loop has a wavelength much larger than the size of the fine-scale turbulence. This separation of length scales justifies the use of a turbulence closure model. In cylindrical coordinates r, ϕ, and x, the dimensionless governing equations are [length scale $= D$ (nozzle exit diameter), velocity scale $= a_\infty$ (ambient sound speed), timescale $= D/a_\infty$, density scale $= \rho_\infty$ (ambient gas density), pressure scale $= \rho_\infty a_\infty^2$, temperature scale $= T_\infty$ (ambient gas temperature), scale for stresses and k is a_∞^2, and those for ε and ν_t are a_∞^2/D and $a_\infty D$, respectively]

$$\frac{\partial\rho}{\partial t}+\frac{\partial\rho u}{\partial x}+\frac{\partial\rho v}{\partial r}+\frac{\rho v}{r}+\frac{1}{r}\frac{\partial\rho w}{\partial\phi}=0$$

$$\frac{\partial u}{\partial t}+u\frac{\partial u}{\partial x}+v\frac{\partial u}{\partial r}+\frac{w}{r}\frac{\partial u}{\partial\phi}+\frac{1}{\rho}\frac{\partial p}{\partial x}$$

$$=-\frac{1}{\rho}\left[\frac{\partial}{\partial x}(\rho\tau_{xx})+\frac{\partial}{\partial r}(\rho\tau_{rx})+\frac{1}{r}\frac{\partial}{\partial\phi}(\rho\tau_{x\phi})+\frac{\rho\tau_{rx}}{r}\right]$$

$$\frac{\partial v}{\partial t}+u\frac{\partial v}{\partial x}+v\frac{\partial v}{\partial r}+\frac{w}{r}\frac{\partial v}{\partial\phi}-\frac{w^2}{r}+\frac{1}{\rho}\frac{\partial p}{\partial r}$$

$$=-\frac{1}{\rho}\left[\frac{\partial}{\partial x}(\rho\tau_{rx})+\frac{\partial}{\partial r}(\rho\tau_{rr})+\frac{1}{r}\frac{\partial}{\partial\phi}(\rho\tau_{rr})+\frac{\rho(\tau_{rr}-\tau_{\phi\phi})}{r}\right]$$

$$\frac{\partial w}{\partial t}+u\frac{\partial w}{\partial x}+v\frac{\partial w}{\partial r}+\frac{w}{r}\frac{\partial w}{\partial\phi}+\frac{vw}{r}+\frac{1}{\rho r}\frac{\partial p}{\partial\phi}$$

$$=-\frac{1}{\rho}\left[\frac{\partial}{\partial x}(\rho\tau_{x\phi})+\frac{\partial}{\partial r}(\rho\tau_{r\phi})+\frac{1}{r}\frac{\partial}{\partial\phi}(\rho\tau_{\phi\phi})+\frac{2\rho\tau_{r\phi}}{r}\right]$$

$$\frac{\partial T}{\partial t}+u\frac{\partial T}{\partial x}+v\frac{\partial T}{\partial r}+\frac{w}{r}\frac{\partial T}{\partial\phi}+(\gamma-1)T\left(\frac{\partial u}{\partial x}+\frac{\partial v}{\partial r}+\frac{v}{r}+\frac{1}{r}\frac{\partial w}{\partial\phi}\right)$$

$$=\gamma(\gamma-1)\varepsilon+\frac{\gamma}{\rho P_r}\left[\frac{\partial}{\partial x}\left(\rho\frac{\partial T}{\partial x}\right)+\frac{\partial}{\partial r}\left(\rho\frac{\partial T}{\partial r}\right)\right.$$

$$\left.+\frac{1}{r^2}\frac{\partial}{\partial\phi}\left(\rho\frac{\partial T}{\partial\phi}\right)+\frac{\rho}{r}\frac{\partial T}{\partial r}\right] \tag{1}$$

$$\gamma p=\rho T$$

$$\frac{\partial k}{\partial t}+u\frac{\partial k}{\partial x}+v\frac{\partial k}{\partial r}$$

$$=-\Omega-\varepsilon+\frac{1}{\sigma_k\rho}\left[\frac{\partial}{\partial x}\left(\rho\nu_t\frac{\partial k}{\partial x}\right)+\frac{\partial}{\partial r}\left(\rho\nu_t\frac{\partial k}{\partial r}\right)+\frac{\rho\nu_t}{r}\frac{\partial k}{\partial r}\right]$$

$$\frac{\partial\varepsilon}{\partial t}+u\frac{\partial\varepsilon}{\partial x}+v\frac{\partial\varepsilon}{\partial r}=-c_{\varepsilon 1}\frac{\varepsilon}{k+k_0}\Omega-c_{\varepsilon 2}\frac{\varepsilon^2}{k+k_0}$$

$$+\frac{1}{\sigma_\varepsilon\rho}\left[\frac{\partial}{\partial x}\left(\rho\nu_t\frac{\partial\varepsilon}{\partial x}\right)+\frac{\partial}{\partial r}\left(\rho\nu_t\frac{\partial\varepsilon}{\partial r}\right)+\rho\frac{\nu_t}{r}\frac{\partial\varepsilon}{\partial r}\right]$$

$$\Omega=\tau_{ij}\frac{\partial u_i}{\partial x_j},\qquad \tau_{ij}=\frac{1}{3}k\delta_{ij}-\nu_t\left(\frac{\partial u_i}{\partial x_j}+\frac{\partial u_j}{\partial x_i}-\frac{2}{3}\frac{\partial u_k}{\partial x_k}\delta_{ij}\right)$$

$$\nu_t=c_\mu\frac{k^2}{\varepsilon+\varepsilon_0}+\frac{\nu}{a_\infty D}$$

where γ is the ratio of the specific heats and ν is the molecular kinematic viscosity. The terms $k_0=10^{-6}$ and $\varepsilon_0=10^{-4}$ are small positive numbers to prevent division by zero. The model constants[12] are taken to be

$$c_\mu=0.0874,\qquad c_{\varepsilon 1}=1.40,\qquad c_{\varepsilon 2}=2.02,\qquad P_r=0.422$$
$$\sigma_k=0.324,\qquad \sigma_\varepsilon=0.377,\qquad \nu/a_\infty D=1.7\times10^{-6} \tag{2}$$

Now the solution in cylindrical coordinates must be a periodic function of ϕ. We will expand the solution variables in Fourier series in ϕ:

$$\begin{bmatrix}\rho\\u\\v\\w\\T\\p\end{bmatrix}=\begin{bmatrix}\rho_0\\u_0\\v_0\\w_0\\T_0\\p_0\end{bmatrix}+\sum_{n=1}^{N}\left(\begin{bmatrix}\rho_n\\u_n\\v_n\\w_n\\T_n\\p_n\end{bmatrix}\cos(n\phi)+\begin{bmatrix}\rho_{-n}\\u_{-n}\\v_{-n}\\w_{-n}\\T_{-n}\\p_{-n}\end{bmatrix}\sin(n\phi)\right) \tag{3}$$

Here, k and ε are turbulence model variables. They are incorporated into the RANS equations to ensure that the mean flow spreading rate is correctly simulated. They are essentially axisymmetric, as is the mean flow. Thus, in this work both k and ε are regarded as axisymmetric. All of the nonaxisymmetric components of the k and the ε model equations are discarded.

Individual equations for the Fourier expansion coefficients are found in a straightforward manner by substitution of Eq. (3) into Eq. (1) and equating terms according to $\cos(n\phi)$ and $\sin(n\phi)$. This partition of terms reduces the three-dimensional problem effectively to a two-dimensional problem in the x–r plane.

B. Grid Design and Computation Scheme

All of the computations are carried out in the x–r plane. The computation domain and grid design are the same as in Refs. 1 and 2. The size of the computation domain is $35D\times 17D$. It is divided into four subdomains with cascading mesh sizes. The subdomain immediately downstream of the nozzle exit, where the jet mixing layer is thin and the jet plume contains a shock cell structure, has the finest mesh: $\Delta x=\Delta r=D/64$. The mesh size of the next subdomain increases by a factor of two. This continues on so that outside the jet where the mesh is the coarsest has a mesh size of $D/8$.

The governing equations of the different Fourier components are discretized by the multiple-size-mesh, multiple-time-step, dispersion-relation-preserving (DRP) scheme.[13] The method is an extension of the DRP scheme of Tam and Webb.[14] Seven-point stencils are used in the entire computation. The extended method is designed specifically for solving multiple-scales problems of which the jet screech problem is an archetypical example. The use of multiple time steps is crucial to the present effort in reducing the run time of the computer codes. Presently, most CAA/computational fluid dynamics schemes use a single-time-step method to advance in time. The time step is determined by the stability requirement of the finest mesh, and, hence, it is very small. Thus, a lot of unnecessary computations are done over the coarse mesh regions. This results in exceedingly long CPU run times.

C. Artificial Selective Damping

As in Refs. 1 and 2, artificial selective damping terms[15] are added to the discretized finite difference equations. In the present study, they are added to the equations of each azimuthal Fourier mode. There are two reasons for adding artificial selective damping to the computation scheme in the present problem. The first is to damp out short spurious numerical waves and to enhance numerical stability near boundaries and surfaces of discontinuity. The second reason is for shock capturing, which is essential to the jet screech problem. In this case, the variable artificial damping method of Tam and Shen[16] is used. The stencil coefficients and design employed here are the same as described in Ref. 1. In implementing the variable artificial damping method, an inverse stencil Reynolds number of 0.35 is used.

D. Radiation, Outflow, and Other Boundary Conditions

To simulate the jet screech phenomenon numerically, one has to solve an exterior domain problem. Because the computation domain is finite, radiation and outflow boundary conditions must be imposed at the artificial boundaries. The radiation boundary conditions with entrainment flow developed in Ref. 17 and used in Refs. 1 and 2 are also appropriate for the three-dimensional jet screech problem. These radiation boundary conditions are

$$\frac{1}{V(\Theta)}\frac{\partial}{\partial t}\begin{bmatrix}\rho\\u\\v\\w\\p\end{bmatrix}+\left(\frac{\partial}{\partial R}+\frac{1}{R}\right)\begin{bmatrix}\rho-\rho_e\\u-u_e\\v-v_e\\w\\p-p_e\end{bmatrix}=0$$

$$V(\Theta)=u_e\cos\Theta+v_e\sin\Theta+\left[a_e^2-(v_e\cos\Theta-u_e\sin\Theta)^2\right]^{\frac{1}{2}} \tag{4}$$

where $R=(x^2+r^2)^{1/2}$ and Θ are the radial distance and polar angle of a spherical polar coordinate system centered at the nozzle exit with the polar axis pointing in the x direction and ρ_e, u_e, v_e, and p_e are the entrainment flow variables at the location where the radiation boundary conditions are imposed. They are found by the method of Ref. 17.

To implement Eq. (4), the equations need to be expanded in Fourier series. This may be done by substituting Eq. (3) into Eq. (4) and equating the Fourier coefficients to zero. It is straightforward to find that the axisymmetric mode ($n=0$) of Eq. (3) satisfies Eq. (4) by itself. All of the higher-order Fourier terms satisfy the same set of equations that are obtained by zeroing out the entrainment flow terms of Eq. (4).

The nonlinearized outflow boundary conditions of Ref. 1 are also used here. However, because the outflow boundary is deliberately placed far downstream, the nonlinear interaction between different modes is expected to be unimportant. Thus, the convection velocity of the outflow boundary condition is replaced by that of the axisymmetric mode ($n=0$) alone. To implement the outflow boundary conditions, they are first separated into Fourier series components as in the case of the radiation boundary conditions.

The inflow and wall boundary conditions of the present problem are identical to those in Ref. 1. Here it is assumed that the jet is circular and that it is issued from a convergent nozzle; the local Mach number is one at the nozzle exit. The nozzle exit or inflow conditions are taken to be axisymmetric even for jets that exhibit flapping mode screech.

In cylindrical coordinates, the governing equations (1) have an apparent singular at $r=0$. Physically, however, the jet behaves well (no singularity) at the jet axis. To ensure that the numerical solution is accurate and well behaved at and around the jet axis, a set of jet axis boundary conditions is needed. In the past, there have been a number of attempts to try to formulate suitable jet axis boundary conditions. Shih et al.[18] suggested the use of the azimuthal average over the values of the variable on the circle $r=\Delta r$ as the value of the variable at the axis. This was implemented in the works of Morris et al.[19,20] However, a careful analysis of this boundary treatment indicates that the accuracy is only of order (Δr). This is very inaccurate. To preserve the high-order accuracy of the solution, a new set of jet axis boundary conditions has been developed in the present investigation. The formulation of these axis boundary conditions is given in the Appendix. This set of boundary treatments is used throughout this investigation.

III. Numerical Results and Comparisons with Experiments

In all of the numerical simulations carried out in this investigation, only the lowest five modes of the Fourier expansion of Eq. (3) are retained. Experimental investigations clearly indicate that jet screech tones are associated either with the axisymmetric mode or the flapping/helical mode. Thus, the five-mode representation should be quite adequate. All of the numerical results reported here were obtained on Silicon Graphics Origin 2200 and 2000 computers with eight parallel processors. The computation starts with zero initial conditions as in Ref. 1. The numerical solution marches in time and, after a while, locks itself onto the screech feedback mode without external interference. The computation continues until a periodic state is attained at a number of monitoring stations. At this stage, the numerical results are measured and analyzed. The following is a summary of the most important directly measured results and their comparisons with experimental measurements.

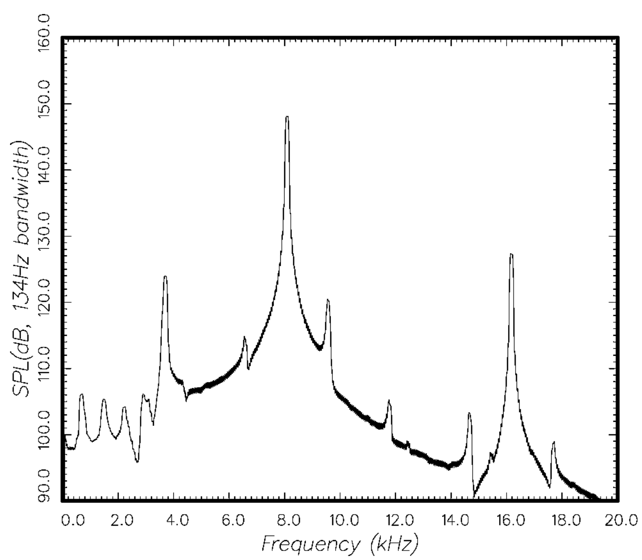

Fig. 1 SPL spectrum from numerical simulation measured at $x = 0.0D$ and $y = 0.642D$; convergent nozzle at $M_j = 1.1$, A_1 mode.

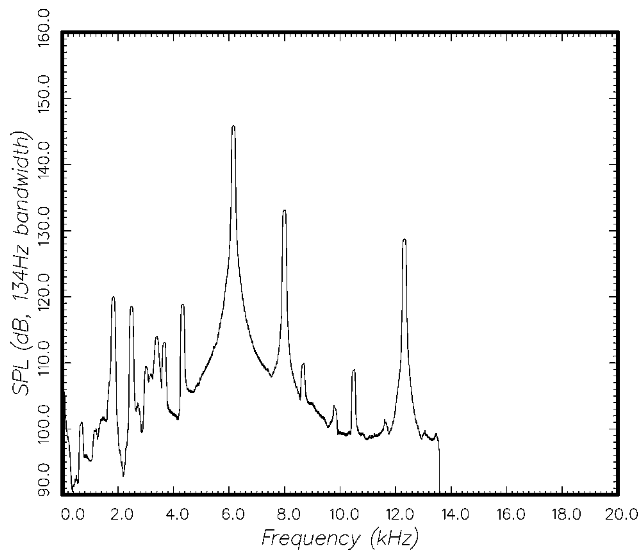

Fig. 2 SPL spectrum from numerical simulation measured at $x = 0.0D$ and $y = 0.642D$; convergent nozzle at $M_j = 1.2$, A_1 and A_2 modes.

Figure 1 shows the sound-pressure-level (SPL) spectrum of a Mach 1.1 jet from a convergent nozzle measured at $x=0.0D$ and $y=0.642D$. The numerical simulation noise spectrum is dominated by a single tone and its first harmonic. It is an axisymmetric, A_1 mode screech at $\lambda/D=1.66$ and 148 dB, where λ is the acoustic wavelength of the screech tone. Figure 2 shows the spectrum of the same jet operating at Mach 1.2. In this case, there are two tones. The dominant tone is an A_1 mode screech at $\lambda/D=2.17$ and 146 dB. The minor tone is from an A_2 screech mode at $\lambda/D=1.67$ and 133 dB. The first harmonic of the dominant tone can also be seen. Here it is appropriate to comment that in physical experiments, sometimes a single tone is observed, whereas at a different jet Mach number two tones are observed. The results of the present simulations are quite consistent with actual experimental experience.[21]

Figure 3 shows the computed SPL spectrum at Mach 1.3. The spectrum consists of a single tone at $\lambda/D=2.78$. The intensity measured at $x=0.0D$ and $y=0.642D$ is 155 dB. Figure 4 shows the azimuthal directivity of this screech tone on a plane located at five jet diameters upstream of the nozzle exit. The radiation pattern resembles that of an acoustic dipole, which is characteristic of a

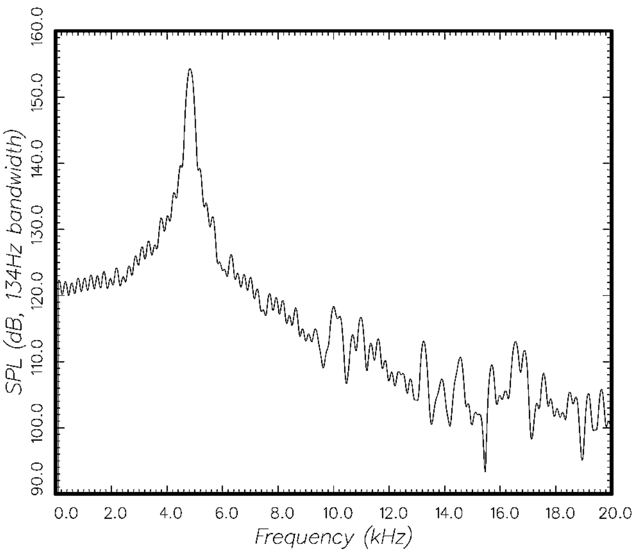

Fig. 3 SPL spectrum from numerical simulation measured at $x = 0.0D$ and $y = 0.642D$; convergent nozzle at $M_j = 1.3$, B mode.

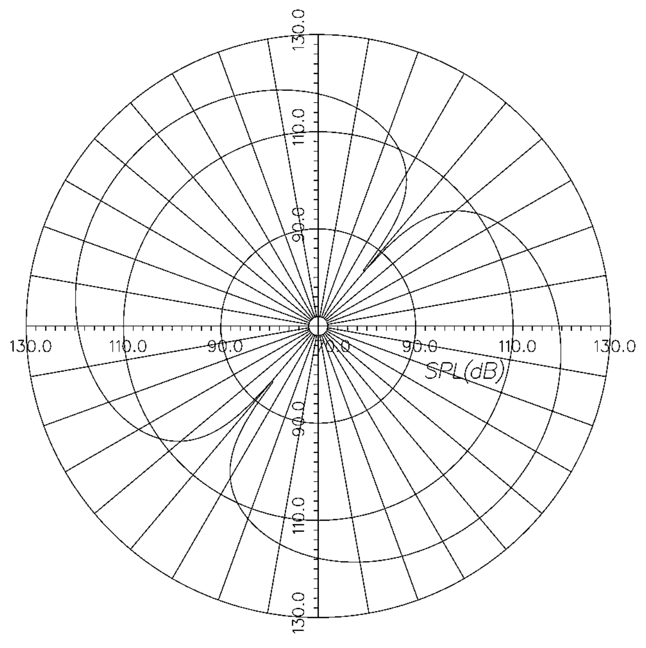

Fig. 4 Directivity plot of SPL at the $x = -5.0D$ plane showing a flapping mode screech; $M_j = 1.3$.

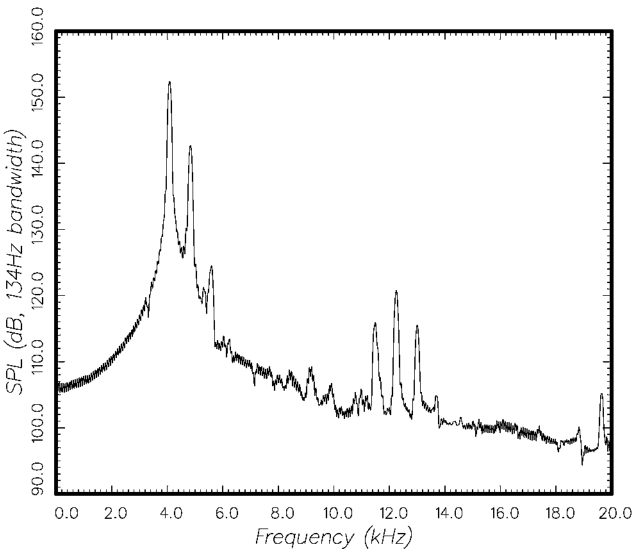

Fig. 5 SPL spectrum from numerical simulation measured at $x = 0.0D$ and $y = 0.642D$; convergent nozzle at $M_j = 1.5$, B and C modes.

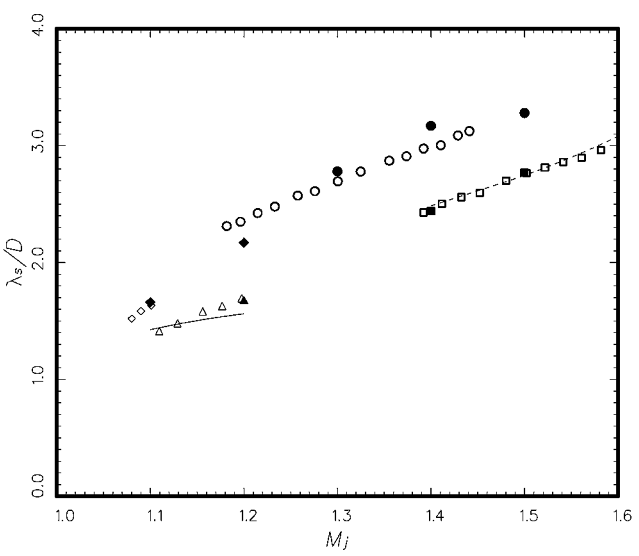

Fig. 6 Comparision between measured and computed screech tone acoustic wavelength to jet diameter ratio: experiment,[6] ◇ = A_1, △ = A_2, ○ = B, and □ = C modes; and numerical simulation, ◆ = A_1, ▲ = A_2, ● = B, and ■ = C modes. Upstream propagating wave: ——, (0, 2) mode and - - -, (1, 1) mode.

flapping screech mode. The screech tone is a B mode. Figure 5 shows the spectrum at an even higher Mach number, $M_j = 1.5$. In this case the spectrum exhibits two tones. The low-frequency tone at $\lambda/D = 3.28$ and 153-dB intensity is a B mode screech. The higher-frequency tone at $\lambda/D = 2.77$ and 142-dB intensity is a C mode. Again, as in actual physical experiments, sometimes both the B and C modes are observed, and at other Mach numbers only one mode is observed.

Figure 6 shows comparisons between the numerically computed ratios of the acoustic wavelength of screech tones to jet exit diameter and those from the experiments of Ponton and Seiner.[6] At low supersonic Mach numbers, $M_j < 1.2$, the screech tones are axisymmetric in the form of the A_1 and A_2 modes. The computed values are in good agreement with experimental data. At higher supersonic Mach numbers, the screech tones switch to the B and C flapping/helical modes. There is again good agreement between the measured and computed values. These comparisons should be judged taking into account the variability of experimentally measured screech data. Previously, Norum[5] compared the frequencies of the A_1, A_2, B, and C modes measured by a number of investigators. It becomes clear when the data were put together that the staging Mach numbers (mode switching) vary from experiment to experiment. It is generally agreed on among experimentalists that the screech phenomenon is extremely sensitive to minor details of the experimental facility and jet operating conditions.

Figure 7 shows the comparisons of tone intensities. In a number of cases, there are two tones. The dominant tone is around 18 dB higher in intensity. Despite this large difference, there are excellent agreements for all of the modes over the entire Mach number range shown in Fig. 7. Even the subdominant tone intensities are in good agreement with experiment.

A point should be made here concerning the numerical predictions contained in Figs. 6 and 7. As far as is known, this is the first numerical prediction of all of the four screech mode frequencies and intensities. Most semi-empirical tone frequency prediction formulas available today are unable to distinguish between the A_1 and A_2 mode or the B and C mode. These formulas offer only a single frequency at a given jet Mach number. As noted before, no tone intensity prediction formula is available (even a totally empirical one). The present prediction of both the dominant and the subdominant tone intensity represents a significant advance in our prediction

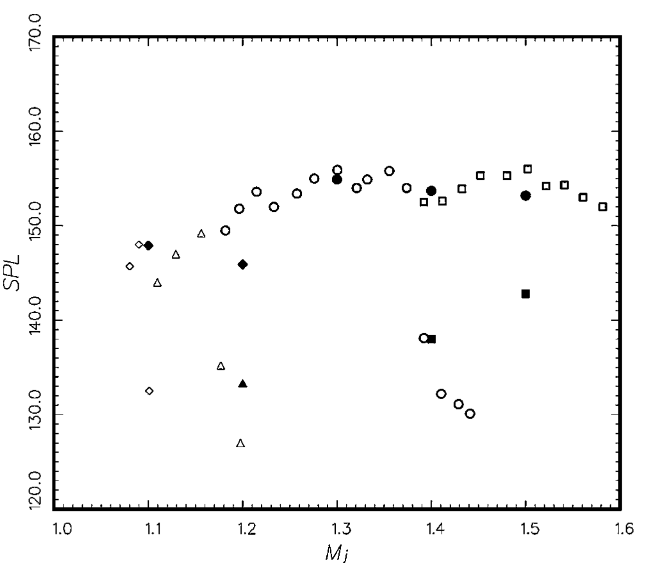

Fig. 7 Comparision between measured and computed screech tone SPL: experiment,[6] ◇ = A_1, △ = A_2, ○ = B, and □ = C modes; and numerical simulation, ◆ = A_1, ▲ = A_2, ● = B, and ■ = C modes.

capability. It also suggests that numerical simulation by CAA methods is a feasible and accurate way to solve highly nonlinear, highly complicated aeroacoustics problems.

IV. Proposed Explanation of the Existence of Two Screech Tones

One important advantage of numerical simulation is that a full set of flow and acoustic data is available. This provides a unique opportunity to test possible explanations/mechanisms that are responsible for the generation of two screech tones at a given jet Mach number. An explanation based on an idea about the feedback processes of the screech feedback loop will be offered hereafter. To provide crucial evidence to support the proposed explanation, data from the numerical simulations will first be analyzed and discussed.

A. Data Analysis

Screech tones are known to be generated by an acoustic feedback loop. The loop is powered by an instability wave of the jet that, when interacted with the shock cell structure around the fourth or fifth shock cell, generates the feedback acoustic disturbance. Let us first measure the shock cell structure and the instability waves. For this purpose, we will use the pressure fluctuations associated with these physical entities. Figure 8a shows the pressure distribution along the centerline of the jet at Mach 1.5 measured at $t = 0.1T$, where T is the screech period. This spatial pressure distribution changes only slightly in time. The reason is that the instability waves, which are time dependent, are basically confined to the shear layer of the jet. They do not affect the centerline pressure appreciably. Figures 8b and 8c are the pressure distribution at $r = 0.3D$ (at $t = 0.35T$) and $r = 0.5D$ (at $t = 0.25T$) in the plane of maximum flapping oscillations. At $r = 0.3D$, the pressure distribution is made up of the pressure fluctuations associated with the shock cells and the instability waves. This is the radial location at which strong interaction between the two takes place. At $r = 0.5D$, the shock cells are weak, and the pressure distribution changes in time as the instability wave propagates downstream.

To determine the shock cell wave number or spacing and those of the instability waves, a Fourier cosine spectral analysis is applied to the instantaneous pressure distribution at $r = 0.0D, 0.3D$, and $0.5D$. The value of pressure at all mesh points of the computation along these lines are used in the spectral computation. The power spectral density (PSD) of the pressure distributions shown in Figs. 8a–8c are given in Figs. 9a–9c, respectively. Here κ is the wave number. Figure 9a consists of a single dominant spike at $\kappa D = 3.907$. This is the wave number of the shock cells. When the measurements are repeated at different times of the screech cycle, it is found that the wave number of the shock cells does not seem to change with time.

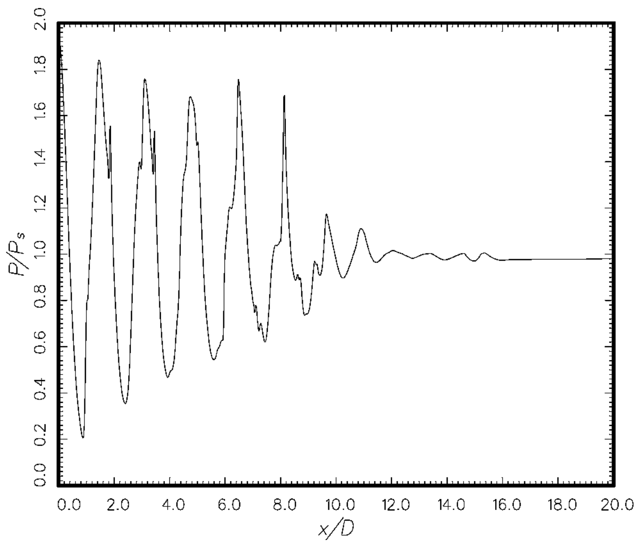

Fig. 8a Pressure distribution along the line $r = 0.0D$ at $t = 0.1T$; $M_j = 1.5$.

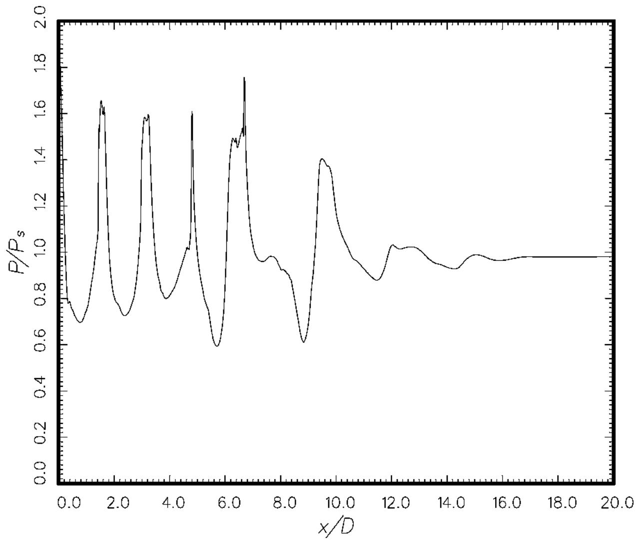

Fig. 8b Pressure distribution along the line $r = 0.3D$ on the maximum flapping mode oscillation plane at $t = 0.35T$; $M_j = 1.5$.

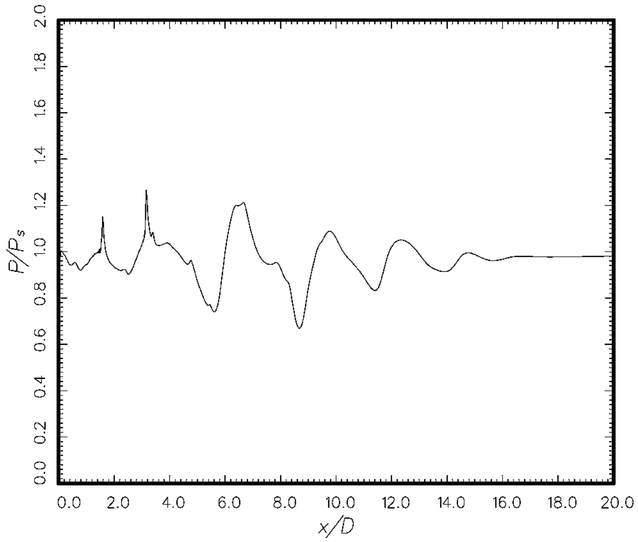

Fig. 8c Pressure distribution along the line $r = 0.5D$ on the maximum flapping mode oscillation plane at $t = 0.25T$; $M_j = 1.5$.

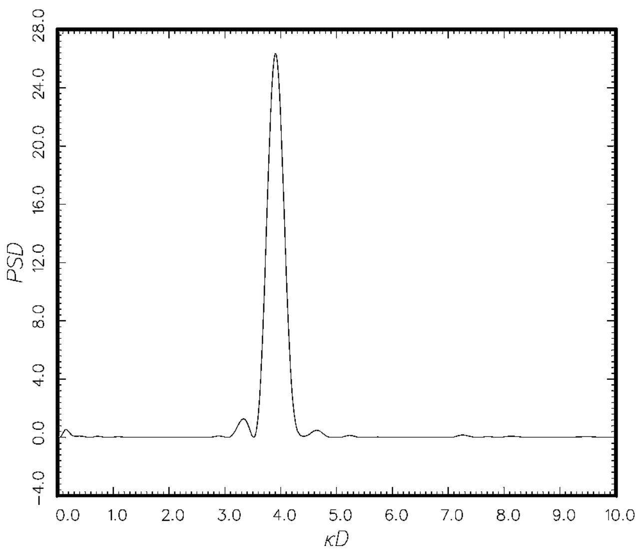

Fig. 9a PSD of the instantaneous pressure distribution along the line $r = 0.0D$ at $t = 0.1T$; $M_j = 1.5$.

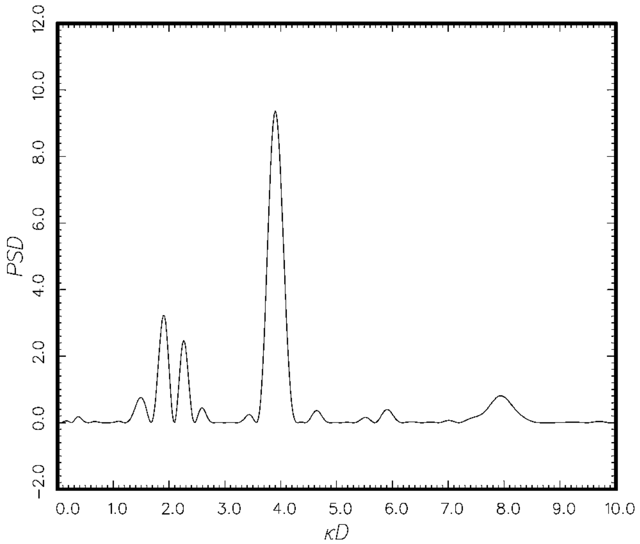

Fig. 9b PSD of the instantaneous pressure distribution along the line $r = 0.3D$ on the maximum flapping oscillation plane at $t = 0.35T$; $M_j = 1.5$.

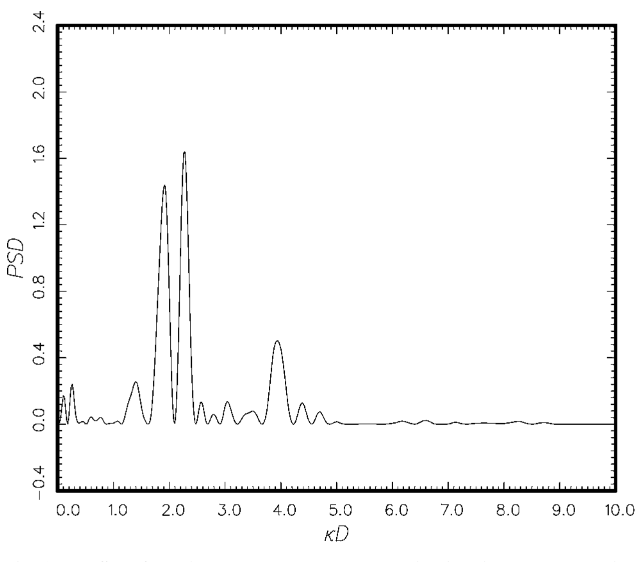

Fig. 9c PSD of the instantaneous pressure distribution along the line $r = 0.5D$ on the maximum flapping oscillation plane at $t = 0.25T$; $M_j = 1.5$.

In Fig. 9b, the PSD consists of three sharp spikes. The main peak at $\kappa D = 3.907$ is that of the shock cell structure. The two smaller peaks are the wave numbers of the instability waves, which are responsible for the generation of the B and C screech modes. In Fig. 9c, the PSD again has three sharp peaks. The one at $\kappa D = 3.907$, which is the smallest of the three, is obviously that of the shock cells. It is relatively weak at this radial location. The other two peaks are those of the instability waves. The wave number of the instability waves do change somewhat over a screech cycle. However, by repeated measurements over time, a time-averaged wave number can be identified. Note that the PSD data offer irrefutable evidence that the two screech tones do coexist simultaneously. In the past, it has been conjectured by some investigators, that two tones appeared in the noise spectrum (a long time measurement) was because the screech mode switched from one to another continuously. It was suggested that there was only one feedback or one screech tone at any instant of time.

Walker et al.[22] performed wavelet analysis of the acoustic signal from a screeching rectangular jet of aspect ratio seven. Based on their wavelet transform data, they concluded that the three screech tones observed in their experiment coexisted simultaneously. This conclusion is consistent with the present finding. However, note that screech tones of large aspect ratio rectangular jets are quite different from those of axisymmetric jets. Rectangular jets support a symmetric and an antisymmetric instability wave mode, whereas circular jets support a host of azimuthal unstable waves. The shock cell structures of these two types of jets are also quite different. Fourier analysis[23] performed on the spatial structure of the shock cells of a large aspect ratio rectangular jet indicated that there were many Fourier modes. For an axisymmetric jet, there is only one dominant Fourier component. These distinct differences in shock cell structure and jet instability characteristics lead to significant difference in the number of screech modes and radiation characteristics for the two types of jets. The measurements of Ref. 23 clearly indicate that, because of the presence of higher-order Fourier shock cell modes, a rectangular jet emits a multitude of screech tones. As many as six modes were reported. For axisymmetric jets only two families of screech modes have been observed. Bearing this in mind, the present finding of the coexistence of two screech modes in choked circular jets is new.

B. Proposed Explanation of Two Coexisting Screech Tones

According to Tam,[8] the energy source of the screech feedback loop is the instability wave of the jet flow. The instability wave is excited by acoustic disturbances near the nozzle lip. It propagates downstream and grows in amplitude. At a distance from four to five shock cells downstream, the instability wave, having attained a large amplitude, interacts with the shock cells. The interaction leads to the emission of acoustic disturbances. Part of the acoustic waves propagate upstream outside the jet. On reaching the nozzle lip, they excite the shear layer and the instability wave. In this way, the feedback loop is closed.

We would like to propose that the interaction between the instability wave and the shock cells is capable of generating two types of acoustic disturbances. Both of them propagate upstream to excite the jet shear layer and the instability wave near the nozzle lip to form a feedback loop. The slight difference in the two ways by which the feedback is accomplished results in a slight difference in the tone frequencies.

Previously Tam et al.[24] suggested a weakest link feedback loop model. This model is based on the analysis of Tam and Tanna.[25] In analyzing the interaction between an instability wave of frequency f and a shock cell structure of wave number K, Tam and Tanna concluded that the coherent scattering of the instability wave in its passage through the periodic shock cells would result in the generation of strong acoustic radiation in a direction θ, where θ is measured from the jet flow direction. The direction θ, the frequency f of the instability wave, and the shock cell wave number K are related by the formula

$$f = Ku_c/2\pi(1 - u_c\cos\theta/a_\infty) \qquad (5)$$

Table 1 Testing the feedback condition[a]

M_j	KD	kD	$2\pi fD/a_\infty$	α	$\lvert\alpha\rvert/KD$
			A_1 and B modes		
1.2	7.535	4.076	3.145	0.282	0.0374
1.3	5.782	3.310	2.260	0.212	0.0367
1.4	4.653	2.500	1.982	0.171	0.0368
1.5	3.907	1.894	1.877	0.136	0.0348
			A_2 and C modes		
1.1	10.73	5.498	3.785	1.449	0.1350
1.2	7.535	4.835	3.670	−0.970	0.1287
1.5	3.907	2.240	2.168	−0.501	0.1282

[a] M_j = jet Mach number, K = shock cell wave number, k = instability wave number, f = feedback acoustic wave frequency, and $\alpha = KD - kD - 2\pi f/a_\infty$.

where u_c is the phase velocity of the instability wave and a_∞ is the ambient sound speeds. The weakest link model suggests that the feedback acoustic wave is the weakest link of the feedback loop. To be able to maintain the feedback, the screech frequency must be such that the strongest radiation is in the direction of the nozzle lip. That is, θ is equal to π if f is the screech frequency. The phase velocity u_c is related to the wave number of the instability wave k by

$$u_c = 2\pi f/k \tag{6}$$

Under the assumption of $\theta = \pi$ in Eq. (5) and using Eq. (6), the feedback relationship becomes

$$KD - kD + 2\pi(fD/a_\infty) = 0 \tag{7}$$

In the preceding weakest link feedback model, the acoustic waves propagate freely upstream outside the jet.

As a simple test if, indeed, the weakest link feedback loop is responsible for the generation of one of the observed screech tones, the measured shock cell wave number K, the instability wave number k, and the screech tone frequency f are substituted into the left-hand side of Eq. (7). Table 1 shows the numerical results at jet Mach number from 1.1 to 1.5. For the A_1 and B modes (see Fig. 6), Eq. (7) is satisfied with an error of less than 4% (last column of Table 1). This is quite remarkable, considering that the screech phenomenon is highly unsteady. For the A_2 and C modes, Eq. (7) is not satisfied. There is a consistent error of about 12%. We propose that the weakest link feedback loop is the one responsible for the generation of the A_1 and B screech modes. Another mechanism is responsible for completing the feedback of screech modes A_2 and C.

In their study of tones from impinging jets, Tam and Ahuja[26] proposed that the feedback disturbances that propagated from the impinging region on the impingement plate back to the nozzle exit was an acoustic mode of the jet flow. These acoustic modes are not freely propagating sound waves. They were found previously by Tam and Hu[27] in a general study of the instability waves and acoustic modes of the jet flow. For subsonic impinging jets, the feedback acoustic mode is confined inside the jet by the mixing layer as it propagates upstream. For a supersonic jet, the acoustic mode propagates outside the jet in the upstream direction guided by the jet. Here we propose that this same feedback acoustic mode of the impinging jet is also excited by the interaction of the instability wave and the shock cell structure. This acoustic mode provides the feedback link of the second feedback loop. This loop is responsible for the generation of the A_2 and C screech tones. One special property of this feedback acoustic mode is that its frequency is restricted to a very narrow band. For the wave mode that propagates upstream at sonic speed following the boundary of the jet, its frequency can easily be calculated using a vortex sheet jet model as described by Tam and Ahuja.[26] For the axisymmetric mode, the lowest frequency is given by the (0, 2) mode. For the flapping/helical mode, the lowest frequency is given by the (1, 1) mode. The calculated acoustic wavelengths of these modes (or a_∞/f, where f is the frequency) as a function of jet Mach number are plotted in Fig. 6. In calculating these results, the diameter of the vortex sheet jet is taken to be equal to the fully expanded jet diameter D_j. The relationship between D_j and the physical nozzle exit diameter D can be found in Ref. 23. As can be seen, the calculated acoustic wavelengths of the screech tones based on the frequency of the feedback acoustic mode are in good agreement with the experimental measurements of Ponton and Seiner[6] for the A_2 and C screech modes. The good agreement obviously provides strong support for the proposed feedback model. Thus, there are two mechanisms to complete the feedback. This is the reason the coexistence of two screech tones is observed.

V. Conclusions

In this work, three-dimensional numerical simulations of a screeching jet from a convergent nozzle over a wide range of Mach numbers have been successfully carried out. It represents a significant advance in the prediction methodology of the screech phenomenon. The numerical simulation reproduces the four experimentally observed screech modes, namely, the two axisymmetric modes A_1 and A_2 and the two flapping/helical modes B and C. The calculated screech frequencies and intensities are in good agreement with experimental measurements. As far as is known, this is the first time computational prediction of screech tones has achieved this level of success.

The availability of a complete set of flow and acoustic field data from numerical simulation provides a rare opportunity to obtain a better understanding of the physics of the screech tone generation processes, especially in regard to the existence of two tones at a given jet Mach number. When PSD analysis of the instantaneous pressure field is performed, unambiguous evidence is found indicating that, whenever two screech tones are measured in the noise spectrum, the two tones coexist at the same time. It repudiates the suggestion offered by some previous investigators that the two tones in the noise spectrum is due to long time averaging of the continuous switching of one screech mode to another and that there is only one tone at a given instant of time.

An explanation as to why there are two coexisting screech tones is proposed. It is suggested that there are two ways for the feedback acoustic disturbances to complete the screech feedback loop. One is by coherent scattering of the instability wave by the quasi-periodic shock cell structure in the jet plume. The other is by an upstream propagating acoustic mode of the jet flow. Evidence from the numerical simulation data as well as theoretical model results are found to strongly support the two proposed feedback mechanisms.

Note that CAA methodology has played a crucial role in making the present investigation possible. It is envisioned that by using a slight extension of the present computation method, it would be feasible to study the generation and propagation of even more complex shock-related jet noise phenomena including broadband shock associated noise. A CAA-based computational approach would allow a direct prediction of the noise spectrum and directivity without empirical constants or adjustments. Furthermore, it would provide complete sets of data for a thorough investigation of the physical processes involved.

Appendix: Jet Axis Boundary Conditions

In this Appendix, the method of analytic continuation is used to formulate a set of numerical boundary treatment at the jet axis when cylindrical coordinates are used.

The flowfield of a jet supports a host of large-scale instability wave solutions. Near the jet axis, in the core region, the amplitudes of the instability waves are usually quite small so that they can be well represented by linear solutions. The linearization may be performed locally on a uniform mean flow, that is,

$$u = \bar{u}, \qquad \bar{v} = \bar{w} = 0, \qquad \rho = \bar{\rho}, \qquad p = \bar{p}, \qquad T = \bar{T}$$

where $u = \bar{u}$ is a constant. The linearized equations of motions are

$$\frac{\partial \rho}{\partial t} + \bar{u}\frac{\partial \rho}{\partial x} + \bar{\rho}\nabla \cdot \boldsymbol{v} = 0 \tag{A1}$$

$$\frac{\partial \boldsymbol{v}}{\partial t} + \bar{u}\frac{\partial \boldsymbol{v}}{\partial x} = -\frac{1}{\bar{\rho}}\nabla p + \nu_t \nabla^2 \boldsymbol{v} \tag{A2}$$

$$\bar{\rho} c_v \left(\frac{\partial T}{\partial t} + \bar{u}\frac{\partial T}{\partial x}\right) + \bar{p}\nabla \cdot \boldsymbol{v} = k_t \nabla^2 T \tag{A3}$$

$$p = \bar{\rho} RT + \rho R\bar{T} \tag{A4}$$

where ν_t and k_t are the turbulent kinematic viscosity and thermal conductivity, respectively.

It can easily be shown that, when Eqs. (A1–A4) are written in cylindrical coordinates (r, ϕ, x), it is an eighth-order system in r. Four of the solutions are bounded at $r = 0$. The other four are unbounded. Here, interest is confined to the bounded solutions alone.

In general, the velocity vector can be represented by a scalar and a vector potential, that is,

$$\boldsymbol{V} = \nabla\Phi + \nabla \times \boldsymbol{A} . \tag{A5}$$

For Eqs. (A1–A4), the solutions for the scalar and vector potentials can be obtained separately. It turns out that the viscous solutions are only related to the vector potential. For convenience, we will refer the vector potential solutions as the (turbulent) viscous solutions.

Scalar Potential Solutions

There are four scalar potential solutions. They can be found by replacing $\boldsymbol{v}$ by $\nabla\Phi$ in Eqs. (A1–A4) and applying Fourier–Laplace transforms to x and t and expanding ϕ dependence in a Fourier series, for example,

$$\Phi(r, \phi, x, t) = \sum_{n=-\infty}^{\infty} \int_{-\infty}^{\infty} \int_{\Gamma} \tilde{\Phi}_n(r, k, w) \times \exp[i(kx - wt + n\phi)] \,\mathrm{d}w \,\mathrm{d}k$$

This leads to a fourth-order differential system in r. The two solutions bounded at $r = 0$ can be expressed in terms of Bessel function of order n. The complete solutions can be written out in full as follows:

$$\tilde{u}_n = ikJ_n(\lambda_\pm r), \qquad \tilde{v}_n = \frac{\mathrm{d}}{\mathrm{d}r} J_n(\lambda_\pm r)$$

$$\tilde{w}_n = \frac{in}{r} J_n(\lambda_\pm r), \qquad \tilde{\rho}_n = \frac{i\,\bar{\rho}\left(\lambda_\pm^2 + k^2\right)}{(w - \bar{u}k)} J_n(\lambda_\pm r)$$

$$\tilde{p}_n = \bar{\rho}\left[i(w - \bar{u}k) - \nu_t\left(\lambda_\pm^2 + k^2\right)\right] J_n(\lambda_\pm r)$$

$$\tilde{T}_n = \left[\frac{i(w - \bar{u}k)}{R} - \left(\lambda_\pm^2 + k^2\right)\left(\frac{i\,\bar{T}}{w - \bar{u}k} + \frac{\nu_t}{R}\right)\right] J_n(\lambda_\pm r) \tag{A6}$$

where

$$\lambda_\pm = \left[\frac{\alpha \pm (\alpha^2 + 4\beta)^{\frac{1}{2}}}{2} - k^2\right]^{\frac{1}{2}}$$

$$\alpha = \frac{ik_t(w - \bar{u}k)/R - \bar{p} - c_v\,\bar{\rho}\,\bar{T} + ic_v\,\bar{\rho}\,\nu_t[(w - \bar{u}k)/R]}{k_t[\nu_t/R + i\,\bar{T}/(w - \bar{u}k)]}$$

$$\beta = \frac{-\bar{\rho}c_v(w - \bar{u}k)^2}{Rk_t[\nu_t/R + i\,\bar{T}/(w - \bar{u}k)]}$$

Viscous (Turbulent) Solutions

There are two sets of viscous solutions. The first set is found by letting

$$\boldsymbol{A} = \psi\,\boldsymbol{e}_x, \qquad p = \rho = T = 0 \tag{A7}$$

where $\boldsymbol{e}_x$ is the unit vector in the x direction. Again, by the use of Fourier–Laplace transform and Fourier expansion, the solution bounded at $r = 0$ is

$$\tilde{p}_n = \hat{\rho}_n = \tilde{T}_n = \tilde{u}_n = 0$$

$$\tilde{v}_n = \frac{in}{r} J_n\left\{i\left[k^2 - \frac{i(w - \bar{u}k)}{\nu_t}\right]^{\frac{1}{2}} r\right\}$$

$$\tilde{w}_n = -\frac{\mathrm{d}}{\mathrm{d}r} J_n\left\{i\left[k^2 - \frac{i(w - \bar{u}k)}{\nu_t}\right]^{\frac{1}{2}} r\right\} \tag{A8}$$

The second set may be found by letting

$$\boldsymbol{A} = \chi\,\boldsymbol{e}_r - i\chi\,\boldsymbol{e}_\phi, \qquad p = \rho = T = 0 \tag{A9}$$

After some algebra, the bounded solution is found to be

$$\tilde{p}_n = \tilde{\rho}_n = \tilde{T}_n = 0$$

$$\tilde{u}_n = -i\left(\frac{\mathrm{d}}{\mathrm{d}r} J_{n+1}\left\{i\left[k^2 - \frac{i(w - \bar{u}k)}{\nu_t}\right]^{\frac{1}{2}} r\right\} + \frac{n+1}{r} J_{n+1}\left\{i\left[k^2 - \frac{i(w - \bar{u}k)}{\nu_t}\right]^{\frac{1}{2}} r\right\}\right)$$

$$\tilde{v}_n = -kJ_{n+1}\left\{i\left[k^2 - \frac{i(w - \bar{u}k)}{\nu_t}\right]^{\frac{1}{2}} r\right\}$$

$$\tilde{w}_n = ikJ_{n+1}\left\{i\left[k^2 - \frac{i(w - \bar{u}k)}{\nu_t}\right]^{\frac{1}{2}} r\right\} \tag{A10}$$

Analytic Continuation into the $r < 0$ Region

The general solution is a linear combination of the scalar and vector potential solutions. The Bessel functions of these solutions can be continued analytically into the nonphysical region of $r < 0$. For positive r, the analytic continuation formula for integer-order Bessel functions is

$$J_n(-\xi r) = (-1)^n J_n(\xi r) \tag{A11}$$

By means of Eq. (A11) and the preceding general solution, it is straightforward to establish

$$\rho_n(-r, x, T) = (-1)^n \rho_n(r, x, t)$$

$$p_n(-r, x, t) = (-1)^n p_n(r, x, t)$$

$$T_n(-r, x, t) = (-1)^n T_n(r, x, t)$$

$$u_n(-r, x, t) = (-1)^n u_n(r, x, t)$$

$$v_n(-r, x, t) = (-1)^{n+1} v_n(r, x, t)$$

$$w_n(-r, x, t) = (-1)^{n+1} w_n(r, x, t) \tag{A12}$$

where ρ_n, p_n, etc., are the amplitude functions of the Fourier series expansion in ϕ.

Here we propose to use Eq. (A12) to extend the solution into the nonphysical negative r region to facilitate the computation of the high-order large-stencil finite difference in r for points adjacent to the jet axis. It is noted, however, that for $n = 1$,

$$\lim_{r\to 0} v_1(r, x, t) \neq 0, \qquad \lim_{r\to 0} w_1(r, x, t) \neq 0$$

For this reason, terms such as v_1/r and w_1/r cannot be computed at the jet axis $r = 0$. Thus, it is recommended that the values of v, w, and all of the other variables not be computed directly by the finite difference equations at $r = 0$. Instead, after the numerical solution is found at the end of nth time step, except for the mesh points in $r \leq 0$, analytic continuation is applied to determine the unknowns at all points in $r < 0$. The values of the variables at $r = 0$ are then calculated by using high-order symmetric interpolation.[28]

Acknowledgments

This work was supported by NASA John H. Glenn Research Center at Lewis Field Grant NAG 3-2102. Computing time was provided by the U.S. Air Force Research Laboratory (through Michael Stanek) and the Silicon Graphics Origin 2200 computer of Florida State University.

References

[1] Shen, H., and Tam, C. K. W., "Numerical Simulation of the Generation of Axisymmetric Mode Jet Screech Tones," *AIAA Journal*, Vol. 36, No. 10, 1998, pp. 1801–1807.

[2] Shen, H., and Tam, C. K. W., "Effects of Jet Temperature and Nozzle Lip Thickness on Screech Tones," *AIAA Journal*, Vol. 38, No. 5, 2000, pp. 762–767.

[3] Powell, A., "On the Mechanism of Choked Jet Noise," *Proceedings of the Physical Society, London*, Vol. 66, 1953, pp. 1039–1056.

[4] Westley, R., and Woolley, J. H., "An Investigation of the Near Noise Fields of a Choked Axisymmetric Air Jet," *Proceedings of AFOSR-UTIAS Symposium on Aerodynamic Noise*, Univ. of Toronto Press, Toronto, ON, Canada, 1968, pp. 147–167.

[5] Norum, T. D., "Screech Suppression in Supersonic Jets," *AIAA Journal*, Vol. 21, No. 2, 1983, pp. 235–240.

[6] Ponton, M. K., and Seiner, J. M., "The Effects of Nozzle Exit Lip Thickness on Plume Resonance," *Journal of Sound and Vibration*, Vol. 154, No. 3, 1992, pp. 531–549.

[7] Raman, G., "Advances in Understanding Supersonic Jet Screech," AIAA Paper 98-0279, Jan. 1998.

[8] Tam, C. K. W., "Supersonic Jet Noise," *Annual Review of Fluid Mechanics*, Vol. 27, 1995, pp. 17–43.

[9] Tam, C. K. W., Seiner, J. M., and Yu, J. C., "Proposed Relationship Between Broadband Shock Associated Noise and Screech Tones," *Journal of Sound and Vibration*, Vol. 110, No. 2, 1986, pp. 309–321.

[10] Tam, C. K. W., "Jet Noise Generated by Large Scale Coherent Motion," *Aeroacoustics of Flight Vehicles: Theory and Practice*, Vol. 1, edited by H. H. Hubbard, NASA RP-1258, 1991, pp. 311–390.

[11] Massey, K. C., and Ahuja, K. K., "Screech Frequency Prediction in Light of Mode Detection and Convection Speed Measurements for Heated Jets," AIAA Paper 97-1625, May 1997.

[12] Thies, A. T., and Tam, C. K. W., "Computation of Turbulent Axisymmetric and Nonaxisymmetric Jet Flows using the k–ε Model," *AIAA Journal*, Vol. 34, No. 2, 1996, pp. 309–316.

[13] Tam, C. K. W., and Kurbatskii, K. A., "Multiple-Size-Mesh Multiple-Time-Step Dispersion-Relation-Preserving Scheme for Multiple Scales Aeroacoustics Problems," *International Journal of Computational Fluid Dynamics* (to be published).

[14] Tam, C. K. W., and Webb, J. C., "Dispersion-Relation-Preserving Finite Difference Schemes for Computational Acoustics," *Journal of Computational Physics*, Vol. 107, Aug. 1993, pp. 262–281.

[15] Tam, C. K. W., Webb, J. C., and Dong, Z., "A Study of the Short Wave Components in Computation Acoustics," *Journal of Computational Acoustics*, Vol. 1, March 1993, pp. 1–30.

[16] Tam, C. K. W., and Shen, H., "Direct Computation of Nonlinear Acoustic Pulses Using High-Order Finite Difference Schemes," AIAA Paper 93-4325, Oct. 1993.

[17] Tam, C. K. W., "Advances in Numerical Boundary Conditions for Computational Aeroacoustics," *Journal of Computational Acoustics*, Vol. 6, Dec. 1998, pp. 377–402.

[18] Shih, S. H., Hixon, R., and Mankbadi, R. R., "Three-Dimensional Structure in a Supersonic Jet: Behavior Near Centerline," AIAA Paper 95-0681, Jan. 1995.

[19] Morris, P. J., Wang, Q., Long, L. N., and Lockard, D. P., "Numerical Predictions of High-Speed Jet Noise," AIAA Paper 97-1598, May 1997.

[20] Morris, P. J., Scheidegger, T. E., and Long, L. N., "Jet Noise Simulations for Circular Nozzles," AIAA Paper 2000-2080, June 2000.

[21] Ponton, M. K., Seiner, J. M., and Brown, M. C., "Near Field Pressure Fluctuations in the Exit Plane of a Choked Axisymmetric Nozzle," NASA TM 113137, Nov. 1997.

[22] Walker, S. H., Gordeyev, S. V., and Thomas, F. O., "A Wavelet Transform Analysis Applied to Unsteady Aspects of Supersonic Jet Screech Resonance," *Experiments in Fluids*, Vol. 22, No. 3, 1997, pp. 229–238.

[23] Tam, C. K. W., Shen, H., and Raman, G., "Screech Tones of Supersonic Jets from Bevelled Rectangular Nozzles," *AIAA Journal*, Vol. 35, No. 7, 1997, pp. 1119–1125.

[24] Tam, C. K. W., Seiner, J. M., and Yu, J. C., "Proposed Relationship Between Broadband Shock Associated Noise and Screech Tones," *Journal of Sound and Vibration*, Vol. 110, No. 2, 1986, pp. 309–321.

[25] Tam, C. K. W., and Tanna, H. K., "Shock Associated Noise of Supersonic Jets from Convergent-Divergent Nozzles," *Journal of Sound and Vibration*, Vol. 81, No. 3, 1982, pp. 337–358.

[26] Tam, C. K. W., and Ahuja, K. K., "Theoretical Model of Discrete Tone Generation by Impinging Jets," *Journal of Fluid Mechanics*, Vol. 214, 1990, pp. 67–87.

[27] Tam, C. K. W., and Hu, F. Q., "On the Three Families of Instability Waves of High-Speed Jets," *Journal of Fluid Mechanics*, Vol. 201, 1989, pp. 447–483.

[28] Tam, C. K. W., and Kurbatskii, K. A., "A Wavenumber Based Extrapolation and Interpolation Method for Use in Conjunction with High-Order Finite Difference Schemes," *Journal of Computational Physics*, Vol. 157, 2000, pp. 588–617.

P. J. Morris
Associate Editor